IEEE Photonics Journal
An IEEE Photonics Society Publication

Open Access

# Hermitian and Non-Hermitian Mode Coupling in a Microdisk Resonator Due to Stochastic Surface Roughness Scattering

Volume 11, Number 2, April 2019

**Stefano Biasi**
**Fernando Ramiro-Manzano**
**Fabio Turri**
**Pierre-Élie Larré**
**Mher Ghulinyan**
**Iacopo Carusotto**
**Lorenzo Pavesi,** ***Fellow, IEEE***

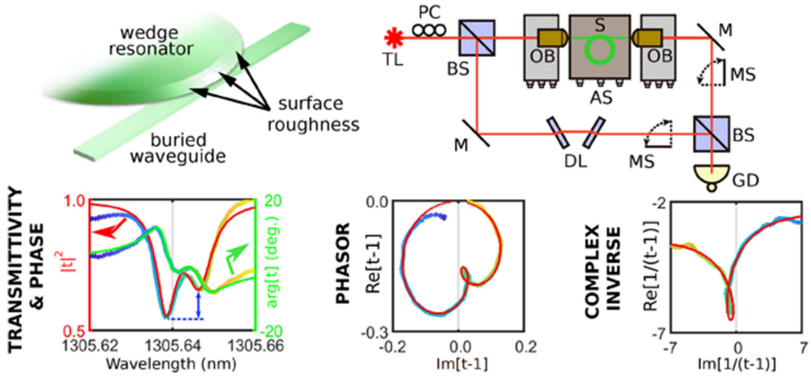


DOI: 10.1109/JPHOT.2018.2880281
1943-0655 

# Hermitian and Non-Hermitian Mode Coupling in a Microdisk Resonator Due to Stochastic Surface Roughness Scattering

**Stefano Biasi**,[1] **Fernando Ramiro-Manzano**,[1] **Fabio Turri**,[1] **Pierre-Élie Larré**,[2] **Mher Ghulinyan**,[3] **Iacopo Carusotto**,[4] **and Lorenzo Pavesi**,[1] ***Fellow, IEEE***

[1]Nanoscience Laboratory, Dipartimento di Fisica, University of Trento, 38123 Povo, Italy
[2]Laboratoire de Physique Théorique et Modélisation, Université de Cergy-Pontoise, CNRS, 95302 Cergy-Pontoise CEDEX, France
[3]Advanced Photonics and Photovoltaics, Foundation of Bruno Kessler, 38123 Povo, Italy
[4]INO-CNR BEC Center and Dipartimento di Fisica, Università di Trento, 38123 Trento, Italy

*DOI:10.1109/JPHOT.2018.2880281*


Manuscript received October 3, 2018; revised October 29, 2018; accepted November 5, 2018. Date of publication November 9, 2018; date of current version March 8, 2019. This work was supported in part by the Provincia Autonoma di Trento (PAT) through the call Grandi Progetti 2012: SIQURO, and in part by the Spanish ministry of Economy, Industry and Competitiveness (MINECO) through the program Proyectos de I+D+i para jóvenes investigadores sin vinculación o con vinculación temporal: TEC2015-74405-JIN. F. Ramiro-Manzano is currently with the Instituto de Tecnología Química (CSIC-UPV). 46022 Valencia, Spain. Corresponding authors: Stefano Biasi and Fernando Raminro-Manzano (e-mail: stefano.biasi@unitn.it; ferraman@fis.upv.es).

**Abstract:** We make use of a phase-sensitive set-up to study the light transmission through a coupled waveguide-microdisk system. We observe a splitting of the transmission resonance leading to an unbalanced doublet of dips. The experimental data are analyzed by using a phasor diagram that correlates the real and the imaginary parts of the complex transmission. In addition, detailed features are evidenced by a complex inverse representation of the data that maps ideal resonances into straight lines and split resonances into complicated curves. Modeling with finite element method simulations suggests that the splitting and the unbalance is caused by an induced chirality in the propagation of the optical fields in the microdisk due to the interplay between the stochastic roughness and the intermodal dissipative coupling, which yield an asymmetric behavior. An analytical model based on the temporal coupled mode theory shows that both a reactive and a dissipative coupling of the counter-propagating modes by the surface roughness of the ring resonator are required to quantitatively reproduce the experimental observations and the numerical simulations.

**Index Terms:** Optical resonator, backscattering, integrated optics.

## 1. Introduction

Optical microresonators are one of the most important building blocks of integrated photonics [1]. They are essential devices in several applications ranging from sensing [2], [3], to metrology [4], [5] and to optical communication [6], [7]. The strong light-matter interaction in microresonators dramatically enhances phenomena such as slow light transmission [8], frequency comb generation [9], entangled [10] or multiple-entangled [11] photon generation.

The light storage capacity in microresonators is usually defined by the quality factor $Q$ of the cavity. Several efforts in material engineering, device design and fabrication processes have been made to reduce the radiative and non-radiative loss channels and, correspondingly, increase the $Q$-factor [12], [13]. While high-transparent materials and optimized geometries are affordable and easily adopted, the roughness inherent to the fabrication process represents the typical limiting source of loss in high or ultra-high $Q$-factor microresonators [14]. This effect becomes dominant in high refractive index contrast cavities, such as silicon-based microresonators. Here, the minimization of the mode volume or the high third-order non-linear response represent the desired features [15]. In particular, the light back-scattered by the surface roughnesses excites a counter-propagating optical mode which is degenerate in frequency with the propagating mode. As a result of the repeated back-scattering processes, stationary super-modes are formed between the co-propagating and the counter-propagating modes with a sizeable energy splitting [16]–[18]. In an ideal resonator, this gives rise to a Hermitian back-coupling and then a symmetric transmission doublet [16], [19], [20]. The coupled mode theory (CMT) with an energy-conserving reactive coupling between the propagating modes describes the ideal case.

As shown in [21]–[24], the presence of scatterers placed in the evanescent field of a resonator, can introduce a geometrical-induced non-Hermitian coupling. By carefully adjusting the scatterers position it is possible to control the degree of splitting and achieve counterintuitive feature of non-Hermitian physics [22]. This perturbation can lead to an asymmetric backscattering and an unidirectional emission in the extreme case at a so-called exceptional point. The optical chirality is ensured by the dissipative nature of the back-coupling and does not require the break of the Lorentz reciprocity. In the ideal case, the stochastic nature of the roughness leads to a simple statistical approach which ignores the non-Hermitian behavior of the back-coupling.

However, measurements show an asymmetry between the split resonances in unperturbed resonators [17], [25]. Experimentally, the asymmetry is observed as different intensities associated to the split peaks (unbalance). These observations may be explained by theoretical studies maintaining the postulate of the Hermitian nature of the collective back-coupling. It has been suggested that the asymmetry might be caused by the interaction of the back-reflections at the bus-waveguide/resonator coupling region [17], or by the non-linear Kerr-effect [25].

In this paper, we address this problem in a silicon nitride high Q-factor optical microdisk. We use a novel phase-sensitive set-up to measure both the intensity and the phase-shift of light propagating along a waveguide coupled to the resonator. We demonstrate that the observed unbalanced doublet of transmission dips is the result of a combination of reactive and dissipative coupling due to the roughness of the resonator surface. We show that a simple Hermitian coupling is not enough to describe the physics in multi-mode resonator with a relative high Q-factor ($\sim 10^5$). In addition, we evidence that a key role is played by a non-symmetrical reflection process due to the microscopic structure of the roughnesses which preserves the Lorentz reciprocity of the transmission but influences the stationary super-modes. Specifically, a stochastic distribution of scattering centers on the outer rim of the microresonator causes an asymmetric average behavior of the surface roughness scattering. This asymmetry is connected to the multi-modal nature of the microresonator and originates the observed unbalance.

In Sec. 2 we report the experimental evidence of asymmetric doublets in linear transmission and phase measurements. In Sec. 3 we discuss numerical simulations that reproduce the experimental observations in terms of surface roughness. In the final Sec. 4, we develop an analytical theory that is able to explain the experimental and numerical observations in terms of the combination of reactive and dissipative couplings between the counter-propagating modes due to the surface roughness.

## 2. The Experiments

The samples studied are disk-shaped (400 nm-thick and 50 $\mu$m-diameter) silicon nitride ($Si_xN_y$) wedge microdisk resonators, vertically coupled to a silicon oxynitride ($SiO_xN_y$) bus-waveguide, as

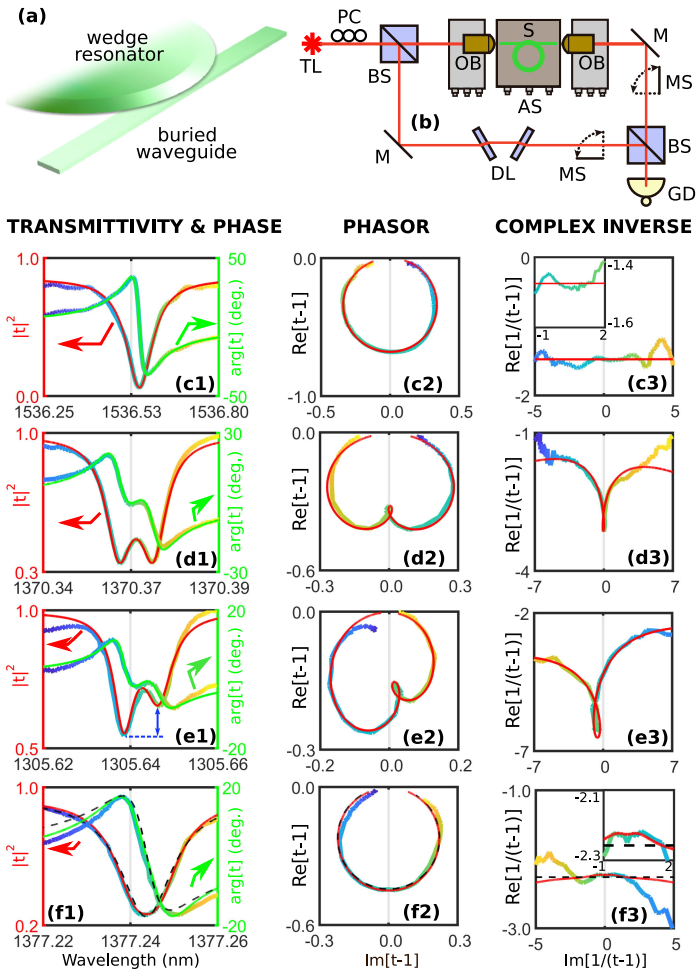


Fig. 1. (a) Sketch of the ring-shaped wedge microresonator device vertically coupled to the bus waveguide. (b) Sketch of the experimental set-up: TL:=Tunable Laser, PC:= Polarization Controller, BS:= Beam Splitter, OB:= Objective, S:= Sample, AS:= Alignment Stage, M:= Mirror, S:= Movable Shutter, DL:= Delay Line and GD:= Germanium Detector. (c) Experimental spectra of the transmitted intensity and phase for a single-mode microresonator with a negligible surface roughness [27]. (d–f) Experimental spectra for the wedge microresonator in different frequency ranges showing a balanced (d), an unbalanced (e), and a hidden (f) doublet. The different columns in (c–f) represent the transmitted intensity and phase as a function of the signal wavelength (c1–f1), the phasor representation (c2–f2) and the inverse complex representation (c3–f3). The colour code (rainbow curves) represents the data as a function of the wavelength (the colour allows to relate the different panels on the same row). The red and green lines display theoretical fits based on the analytical model of Section 4. On panel (e1) we specifically show the intensity unbalance by the arrow and the dashed line.

sketched in Fig. 1(a). Such an optical scheme allows to reach a high quality factor of about $2 \times 10^5$ in a monolithic-integrated optical system [26].

The spectra of the transmitted intensity and the transmission phase-shift as a function of the signal wavelength were measured using a novel phase sensitive set-up based on a free-space Mach-Zehnder interferometer. The bus-waveguide/resonator system is placed into one arm according to the scheme shown in Fig. 1(b). A near-infrared tunable laser is butt-coupled through the bus-waveguide facets by means of two objectives. These are placed on a close-loop three-axis piezoelectric translational stage in order to optimize the coupling and achieve a stable alignment. The signal polarization is controlled at the bus-waveguide input. The interferometer is set in a nearly balanced condition by using a delay system and a mechanical slit as optical attenuator. The tunable laser is swept at 1 nm/s and the transmission through the Mach-Zehnder interferometer is

recorded with a fiber-coupled Germanium ($Ge$) detector. Depending on the position of the shutters, the transmission through either arms of the interferometer, or the interference signal are measured. Systematic and stable measurements are ensured by a full remote control of the interferometer and by enclosing it into a box. The laser intensity is chosen to be weak enough to stay in the linear regime. A complete description of the optical set-up is properly reported in [28].

In a single mode microresonator with a negligible side-wall roughness (for more details see [27]), the transmission response displays a single Lorentzian-shaped resonant feature (see Fig. 1(c1)). On the contrary, our wedge microresonator exhibits clear double resonant peaks in transmission [26] and a double-step jumps in the phase-shift. The three rows Fig. 1(d)–(f) show three examples of transmission and phase-shift spectra in different wavelength ranges, where the mode splitting for different azimuthal modes displays different features. While the doublets observed for high/ultra-high quality-factor and single-mode microresonators [16], [19], [20] consist of a pair of *balanced* peaks of equal intensity, in most cases we observe *unbalanced* doublets formed by a pair of peaks of appreciably different heights (see, e.g., Fig. 1(e1)). To obtain a balanced doublet (see Fig. 1(d)) we had to increase the temperature of the sample. As a consequence, a slightly unbalanced doublet at room temperature is red shifted and it changes casually to a balanced configuration [29]. In addition, by using the phase sensitive set-up, we also evidenced cases where no frequency-split in transmission is visible (Fig. 1(f1)). We name this situation a hidden doublet case. Therefore, we do observe different cases of balanced (d), unbalanced (e) and hidden (f) doublets. A relatively small splitting of the doublets compared to the free spectral range of the microdisk resonator and to the distance to other family of modes is observed. This clearly indicates that they must originate from the coupling of counter-propagating modes with opposite angular momentum in the microdisk.

Another way to look at the mode properties is to use parametric phasor plots (Fig. 1(c2)–(f2)). This representation puts together the real and imaginary part of the transmission amplitude ($t$) as a function of the signal wavelength. The phasor plot has been broadly employed in electrical engineering as a useful analysis tool but has not yet attracted a comparable attention in photonics [19], [30]. Here, we will show that this method is a powerful tool for characterizing the mode splitting and to extract with an extremely high precision the parameters that define the different processes.

In an ideal resonator/waveguide system with no backscattering, only a single forward propagating mode is excited. In this case, the phasor graph represents the typical Lorentzian in transmission with his peculiar phase-shift into a perfect circle (see Fig. 1(c2)). This geometrical identity not only shows the ideality of the optical system, but also allows extracting information on the bus-waveguide-resonator coupling directly from the diameter of the circle. In particular, when the diameter is greater, smaller than, or equal to the unity, the coupling scenario corresponds to over, under or critical coupling regime, respectively. In the presence of resonance splitting due to, e.g., the backscattering, the circle in the phasor representation is significantly deformed. A balanced doublet corresponds to a pair of symmetric lobes as shown in Fig. 1(d2). When the doublet is not balanced, one can see in Fig. 1(e2) that the two lobes acquire different sizes as a result of the asymmetry in the transmission and phase-shift of the split modes. The ratio between the areas of the lobes in the phasor diagram can be taken as a quantitative measure of the unbalance.

In addition, a further powerful analysis is possible by using the two-dimensional nature of the phasor diagram. By performing a complex inversion [31], a circle, which passes through the origin of the phasor diagram (see Fig. 1(c2)), is mapped onto a straight line. Let us define the complex inversion by mapping the data into the complex plane $\left(Re\left(\frac{1}{t-1}\right), Im\left(\frac{1}{t-1}\right)\right)$ - as shown in the third columns of Fig. 1(c–f). Here we confirm that in the case of the single resonance the complex inversion yields a straight line within the experimental errors (Fig. 1(c3)). In this complex inversion representation, even a very small perturbation of the circle in the phasor representation gives rise to a sizeable deformation of its inverse (Fig. 1(d3) and (e3)). More interesting is the case of the hidden doublet. In this case, the side-wall roughnesses cause a resonance split which yields an indiscernible perturbation of the symmetric Lorentzian in transmission or of the perfect circle in the phasor representation. On the contrary, it produces a noticeable peak in the single line of the inverse (Fig. 1(f3)). The strong sensitivity to deformations makes this representation a valuable tool to reveal information which are masked in the conventional resonance analysis. Therefore, this

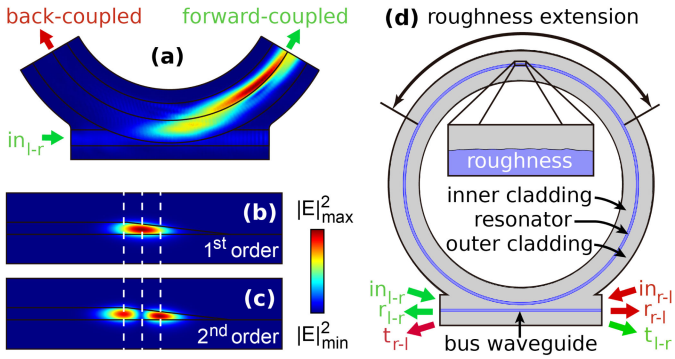


Fig. 2. (a) 3D simulation of the light intensity in the vertical coupling region between the bus-waveguide and the wedge resonator. The field intensity inside the wedge portion reveals a beating pattern between the different radial modes of the wedge resonator [32], [33] that are excited by the forward coupling. The amount of back-scattered light is instead almost negligible. (b)–(c) Field profile of the 1st and 2nd radial modes of the wedge resonator. (d) 2D model of the bus-waveguide-resonator system. The arrows labelled by *in*, *r* and *t* represents the inserted, reflected and transmitted signals, respectively. The indices l-r and r-l refer to the two situations where the input signal light is inserted on the left and propagates from left-to-right (l-r, green arrows) or is inserted on the right and propagates from right-to-left (r-l, red arrows).

method could be applied in various other fields, such as metrology or biosensing, to enhance the sensitivity of devices.

## 3. Simulations

In order to understand the experimental observations, we have performed numerical simulations of the bus-waveguide/wedge microdisk system. These simulations were based on the finite elements method (FEM) engine by Comsol Multiphysics controlled by the mathematical programming environment of Matlab.

As a first step, we made use of a full 3D model of the device to study the back-reflections connected to the vertical coupling between the bus-waveguide and the wedge shaped microdisk. As it is shown in Fig. 2(a), almost all the coupled light propagates in the forward direction inside the resonator and back-reflections into oppositely propagating modes have an almost negligible amplitude. This is due to the fact that the light entering the coupling area experiences a smooth growth of the wedge profile (7 degree), so it progressively couples to the resonator with almost no reflections. Quantitatively, the back-scattered intensity ($S_{sc}$) with respect to the forward scattered intensity ($S_{forward}$) amounts to $S_{sc}/S_{forward} = 2 \times 10^{-3}$ distributed over all the supported modes. Based on this result, we will focus our attention on mode coupling effects that are due to the microdisk resonator, in particular to the roughness of its surface.

A fully 3D simulation of the system is computationally out of our means, therefore we used a simplified 2D model including a ring resonator coupled to a waveguide, as sketched in Fig. 2(d). In contrast to the overwhelming computational cost of the 3D calculations, this simplified 2D model allows performing large scale statistical studies (with up to $10^4$ simulations) of highly detailed geometries containing nanometric-size surface roughness. The microring geometry has been chosen to select different radial modes, allowing for single-(multi-)mode operation for a waveguide width of 0.53 $\mu$m (0.7$\mu$m). A $Si_3N_4/SiO_2$ platform with refractive indexes equal to 2, 2 and 1.45 for the resonator, bus-waveguide and surrounding media has been used. As in the experiment, the large radius of curvature of 25 $\mu$m allows neglecting bending losses as well as back-reflections from the bus-waveguide/resonator coupling area. For the configuration under examination, these latter amount to $S_{sc}/S_{forward} \approx 2 \times 10^{-8}$ or $10^{-6}$, for single- or multi-mode resonators, respectively. Therefore, the simulations are based on the assumption that the back-scattering process responsible for the coupling between the counter-propagating modes and, then, for the unbalanced doublets is

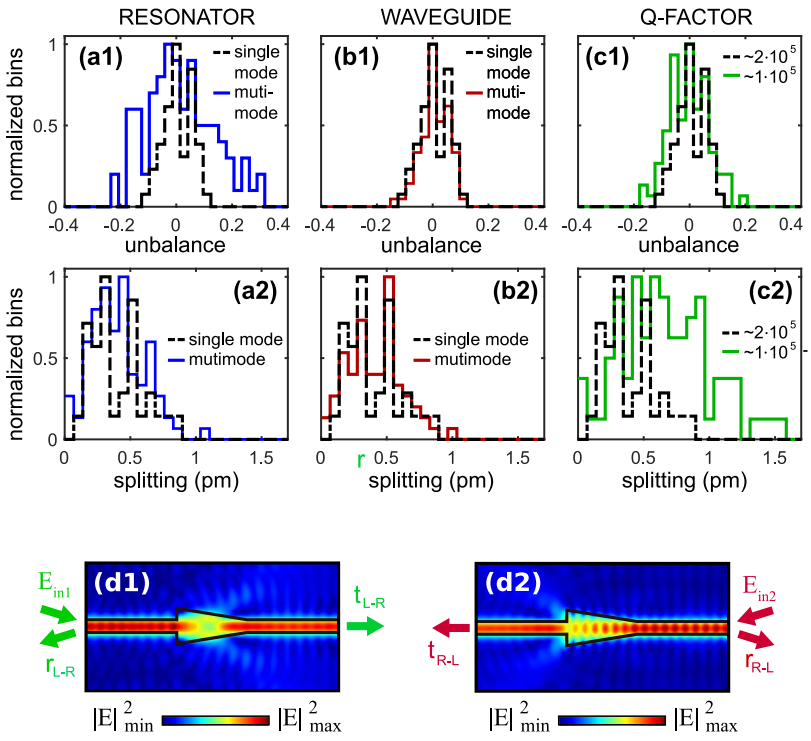


Fig. 3. Panels (a–c): Normalised histograms of the peak unbalance (a1–c1) and of the mode splitting (a2–c2) in different cases: when the resonator (a) or the waveguide (b) are changed from single- to multi-mode (black dashed and coloured solid lines, respectively), and when the Q-factor of the single-mode resonator is halved (black dashed line $Q = 2 \times 10^5$, green solid line $Q = 1 \times 10^5$) (c). Panel (d): Simulation of a non-symmetrical scatterer device inside a single-mode waveguide for light incident from (d1) the left (l-r) or (d2) from the right (r-l). Both cases show the same transmission ($T = 84.48\,\%$) but different reflections ($R_{l-r} = 6.7 \times 10^{-2}\,\%$, $R_{r-l} = 0.674\,\%$).

the roughness on the ring edges. This has been simulated in the 2D model as a disorder in the waveguide width of the ring with a gaussian statistics (root mean square amplitude ranging from 4 to 8.5 nm, and a correlation length of 0.1 $\mu$m). As shown in Fig. 2(d)), the scatterers are distributed over one third of the external rim in the opposite region of the bus-waveguide/ring coupling, so that the coupling region remains isolated from any possible back-scattering source. The roughness determines the intrinsic Q-factor of the device while the gap between the resonator and the waveguide allows imposing a critical coupling condition.

The histograms in Fig. 3(a)–(c) show a statistical study of about 400 realizations of the disorder ($\sim$100 simulations per studied case). These characterize the effect on the mode splitting and on the peak unbalance of different values of the Q-factor and different mono-/multi-radial-modal scenarios. Here, the unbalance is defined as the ratio between the difference in height of the doublet dips and the minimum of the transmittivity. For each choice of parameters, the amount of the splitting and of the unbalance changes stochastically for each realization of the disorder. In particular, the histograms (a1)–(c1) of the unbalance show a symmetry around the origin (confirmed by a very small mean value of about $10^{-3}$). On the other hand, the mode splitting exhibits a net non-zero average value.

Panels (a1–a2) show the effect of increasing the waveguide width in the ring from $w = 0.53\ \mu$m to $w = 0.7\ \mu$m, passing from a single-mode (SM) to a multi-mode (MM) configuration while preserving the Q-factor ($Q \approx 2 \times 10^5$) via an increased amplitude of the roughness. Similar values of the mode splitting are observed ($\overline{ms}_{(MM)}/\overline{ms}_{(SM)} \simeq 1.02$ and $\sigma_{(MM)}/\sigma_{(SM)} \simeq 1.05$, where $\overline{ms}_{(XX)}$ is the average of the distribution of the data for the $XX$ case and $\sigma_{(XX)}$ is its standard deviation), which can be explained by the similar value of the total losses. On the other hand, the magnitude of the

unbalance is strongly increased ($\sigma_{(MM)}/\sigma_{(SM)} \simeq 2.4$) by the presence of more channels for back-reflection and absorption in the multimode resonators.

Panels (b1–b2) represent the same study for an increasing size of the bus-waveguide width, while the gap is reduced to maintain the same Q-factor for the resonator. This allows investigating the role of the back-reflections in the bus-waveguide/resonator coupling area: as expected from previous calculations, the almost-identical results obtained for the single- and multi-modal waveguide case (for both the unbalance $\sigma_{(MM)}/\sigma_{(SM)} \simeq 0.96$ and the mode splitting $\overline{ms}_{(MM)}/\overline{ms}_{(SM)} \simeq 1.04$, $\sigma_{(MM)}/\sigma_{(SM)} \simeq 1.06$) give a further confirmation that the waveguide coupling is not the source of the unbalance in our system.

Panels (c1–c2) represent the effect of an increased roughness amplitude, which reduces the Q-factor from $Q \approx 2 \times 10^5$ to its half value $Q \approx 1 \times 10^5$. As expected, the increased disorder reinforces the backscattering phenomena visible in the amount of unbalance (with a standard deviation ratio of $\sigma_{(Low-Q)}/\sigma_{(High-Q)} \simeq 1.43$) and mode splitting (of mean value of $\overline{ms}_{(Low-Q)}/\overline{ms}_{(High-Q)} \simeq 1.77$ and standard deviation of $\sigma_{(Low-Q)}/\sigma_{(High-Q)} \simeq 1.74$).

In summary, these simulations indicate that the unbalance is negligible in high/ultra-high Q-factor or single-mode resonators, in agreement with the previous literature [16], [19], [20]. On the other hand, the amount of unbalance is increased in multi-mode resonators. The physical mechanism which yields the unbalance is the interplay between scattering and dissipative coupling which, on average, gives rise to an asymmetrical scattering, so that waves propagating in opposite directions interact with the surface defects in a different way. This can be demonstrated by a simple simulation of a scatterer which has a specific asymmetric shape (Fig. 3(d)). In a simple model, we simulate an arrow-like waveguide. In this case the scattering is due to the non adiabatic waveguide width increase and to the asymmetry of the abrupt width reduction. The two panels show the electric field distribution for light incident from different directions: when the input port is swapped, the reflectance $R$ exhibits a marked difference of about one order of magnitude ($R_{l-r} = 6.7 \times 10^{-2}$ % vs $R_{r-l} = 0.67$ %, where the index l-r refers to light that travels from left to right and is reflected back to the left, the index r-l to the opposite situation). This difference in reflectivity is of course compatible with Lorentz reciprocity theorem, which only imposes that the transmittance is the same in the two directions (simulations yield a similar value of $T = 84.48$ %). The reflectance difference is due to the power loss caused by the light scattering out of the propagating waveguide mode. Note that such an asymmetry can not occur in purely reactive single mode resonators where the transmission and reflection are related by energy conservation and the symmetry of the former is imposed by the Lorentz reciprocity theorem. The numerically observed asymmetry of panels (d1–d2) therefore involves dissipative processes. These findings help to understand our experimental observations. Since the two peaks in the doublet originate from a repeated exchange of energy between waves propagating in opposite directions due to reflection, we expect that the average asymmetric reflection, similar to that shown in panels (d1–d2), bears a close relation with the experimentally observed unbalance.

To better understand this link, we have extended our numerical simulations to look at the reflected intensity by the ring resonator. The results are shown in the different panels of Fig. 4. In particular, in the centre and right columns we have compared the reflectivity for light injected on the left (l-r) or on the right (r-l) for different realizations of the disorder which yield different balance in the doublets. As a check of our numerical simulations, we have controlled that in all cases the transmission does not change with the incidence direction, in agreement with the Lorentz reciprocity theorem.

In the absence of any surface roughness, reflectivity of course vanishes independently of the excitation direction. In the presence of a sizeable roughness, reflection acquire a marked asymmetry, typically in association with a marked unbalance in the transmission doublet. Panels (a1–a3) illustrate a case with an almost balanced doublet, where l-r and r-l reflections are very close. Panels (b1–b3) show the case of a markedly unbalanced doublet in the transmission response (b1), which is associated to very different reflection spectra in the two directions (b2–b3). Interestingly, the simulation is also able to correctly model the hidden doublet case. Panels (c1–c3) show that the doublet is completely hidden in the transmission spectra (c1) while the reflectivity is strongly quenched in one direction (c3) and is significant in the other (c2). While the phasor plot, shown in

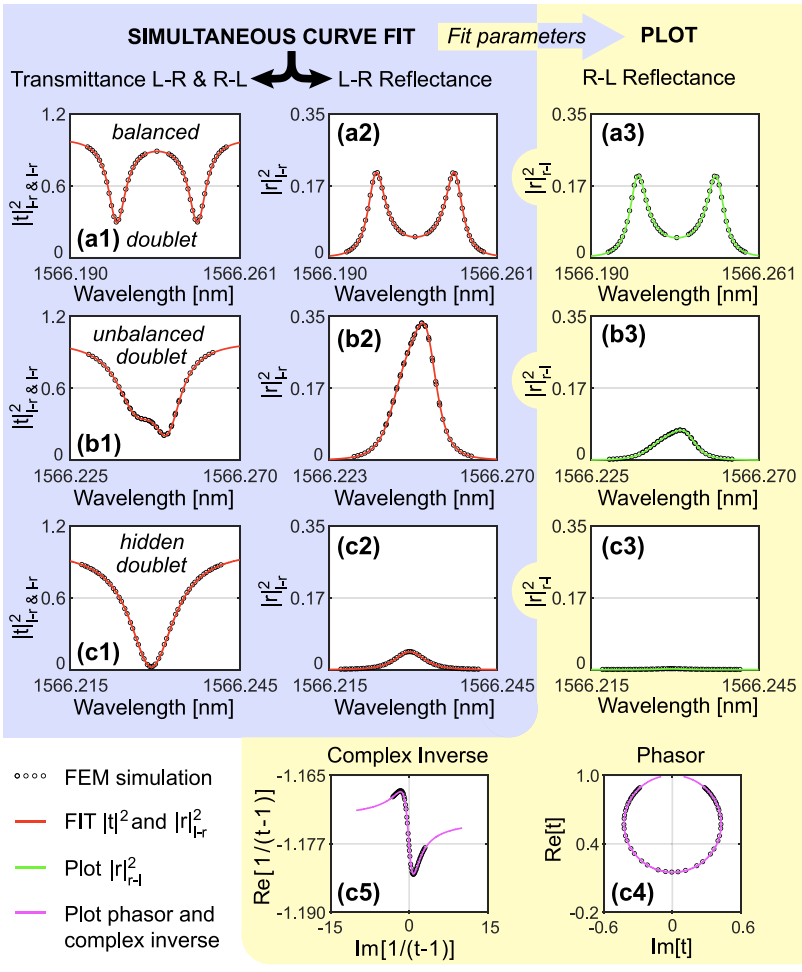


Fig. 4. Transmission (a1–c1), l-r (a2–c2) and r-l (a3–c3) reflection for different realizations of the disorder which yield a balanced doublet (1), an unbalanced doublet (2) and a hidden doublet (3). The black circles are the simulation values while the red line is the fit with the theoretical model of Section 4. For each case, the green curves are obtained by plotting the Eq. 8 for the r-l excitation using the parameters fitted from the l-r ones. While almost invisible in the transmission, the hidden doublet of panel (c1) can be revealed in the complex inverse (c5) of the phasor diagram (c4).

panel (c4), still resembles to the typical circle of a single Lorentzian resonance, the deviation of its inverse (shown in panel (c5)) from a straight line is a clear signature of the back-scattering process. These results support our initial guess that the unbalance is closely related to an asymmetric coupling between the two propagating modes induced by the roughness scattering. Note that such an asymmetric coupling has already been seen in a microdisk with two nanoparticles close to its external rim [22]. In this case, the strength of the backscattering can be different depending on the propagating direction: from clockwise (CW) to counter-clockwise (CCW) or from CCW to CW. In our case, the stochastic nature of the roughness should introduce a statistical approach which leads, on average, to a symmetric backscattering as shown in [16], [19], [20]. However, the repeated back-scattering processes on the surface roughness in a multi-modal resonator is not enough to neglect the possible asymmetric behavior of the several scatterers. This means that the collective action of the scatterers, instead of cancel the phase contribution, could intrinsically lead to the unbalance. One could easily reproduce this behavior following the receipts shown in the histograms (Fig. 3) and therefore without forcing extreme conditions.

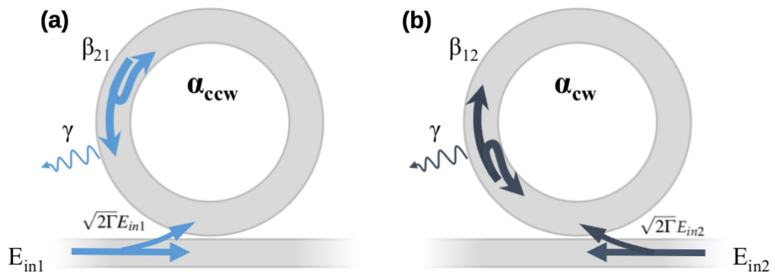


Fig. 5. (a), (b) Sketch of the fields in the the l-r (a panel) and the r-l (b panel) excitation configurations. The different symbols are deinfed in the text.

## 4. Analytical Model

Based on results reported in the previous section, we build an analytical model of the coupled bus-waveguide/resonator device. The numerical simulations will then serve as a benchmark for the theoretical model which is used to understand the experimental observations. Our intuitive analytical model is based on the Temporal Coupled Mode Theory (TCMT) [33]–[37] and the usual properties of a time-reversal-invariant system. Let us consider a resonator coupled to a bus-waveguide as sketched in Fig. 5(a)–(b). The light coming from the input port of the waveguide ($\boldsymbol{E}_{in}$) couples into the microring resonator, which supports two degenerate modes: the CW propagating mode ($\alpha_{cw}$) and the CCW propagating one ($\alpha_{ccw}$).

In the ideal case, where all back-reflections are negligible, only one of the two coupled modes, $\alpha_{ccw}$ and $\alpha_{cw}$, is excited by its corresponding input port: l-r ($E_{in1}$) or r-l ($E_{in2}$). On the other hand, the surface roughness of the microdisk and the non-adiabaticity in the bus-waveguide/microdisk coupling [17], [19] can respectively couple the two counter-propagating modes ($\alpha_{cw} \leftrightarrow \alpha_{ccw}$) and the incident waves to the oppositely propagating resonator modes. The dynamic behaviour of the field amplitudes is described thanks to the :

$$\frac{d\boldsymbol{\alpha}}{dt} = (i\boldsymbol{\Omega} - \boldsymbol{\gamma}^{int} - \boldsymbol{\Gamma}^{ext})\boldsymbol{\alpha} + i\boldsymbol{K}^{T}\boldsymbol{E}_{in}, \tag{1}$$

where the input and output ports are connected by the following equation:

$$\boldsymbol{E}_{out} = \boldsymbol{C}\,\boldsymbol{E}_{in} + i\boldsymbol{K}\,\boldsymbol{\alpha}, \tag{2}$$

with:

$$\boldsymbol{\alpha} = \begin{pmatrix} \alpha_{ccw} \\ \alpha_{cw} \end{pmatrix} \quad \boldsymbol{E}_{in} = \begin{pmatrix} E_{in1} \\ E_{in2} \end{pmatrix} \quad \boldsymbol{E}_{out} = \begin{pmatrix} E_{out1} \\ E_{out2} \end{pmatrix} \quad \boldsymbol{\Omega} = \begin{pmatrix} \omega_1 & 0 \\ 0 & \omega_2 \end{pmatrix} \quad \boldsymbol{\gamma}^{int} = \begin{pmatrix} \gamma_1^{int} & \beta_{12} \\ \beta_{21} & \gamma_2^{int} \end{pmatrix}$$
$$\boldsymbol{C} = \begin{pmatrix} c_{11} & c_{12} \\ c_{21} & c_{22} \end{pmatrix} \boldsymbol{K} = \begin{pmatrix} k_{11} & k_{12} \\ k_{21} & k_{22} \end{pmatrix}. \tag{3}$$

As we have seen in the simulations presented in Sec. 3, the geometry of our system exhibits negligible back-reflections from the bus-waveguide/resonator coupling. Correspondingly, the reflection of the system has to be zero far away from the resonance and, therefore, the scattering matrix reduces $\boldsymbol{C}$ to an identity, $\boldsymbol{C} = \boldsymbol{I}$. Analogously, simulations suggest that the coupling of the incident fields to the oppositely circulating modes has to vanish too, which imposes that $k_{12} = k_{21} = 0$. In the absence of roughness, the CW and CCW propagating modes are related by a specular symmetry, so they have the same bare frequency $\omega_1 = \omega_2 = \omega$, they feel the same intrinsic losses due to material absorption, $\gamma_1^{int} = \gamma_2^{int} = \gamma$, and are identically coupled to the corresponding incident field, $k_{11} = k_{22} = k$.

The situation is different for what concerns the effect of roughness. In the general case, coupling a multi-mode resonator to external baths introduces real and imaginary terms in the resulting mode dynamics [33]. In particular, the coupling parameters $\beta_{12}$ and $\beta_{21}$ can have fully independent values, their Hermitian (related to the conservative exchange of energy between counter-propagating

modes) and non-Hermitian (related to interference effect in the loss processes) parts are generally fully independent from each other. A simple model to understand this crucial issue will be discussed in the following subsection. A direct physical consequence of the difference between $\beta_{12}$ and $\beta_{21}$ is then the difference in the reflection amplitudes shown in Fig. 4.

The coupled mode Eq. 2 for the two different excitations (l-r and r-l) have the following forms:

$$\begin{cases} \dfrac{d\alpha_{ccw}}{dt} = (i\omega - \gamma - \frac{|k|^2}{2})\alpha_{ccw} - \beta_{12}\alpha_{cw} + ikE_{in1} \\ \dfrac{d\alpha_{cw}}{dt} = (i\omega - \gamma - \frac{|k|^2}{2})\alpha_{cw} - \beta_{21}\alpha_{ccw} \end{cases} \tag{4a}$$

and

$$\begin{cases} \dfrac{d\alpha_{cw}}{dt} = (i\omega - \gamma - \frac{|k|^2}{2})\alpha_{cw} - \beta_{21}\alpha_{ccw} + ikE_{in2} \\ \dfrac{d\alpha_{ccw}}{dt} = (i\omega - \gamma - \frac{|k|^2}{2})\alpha_{ccw} - \beta_{12}\alpha_{cw}, \end{cases} \tag{5a}$$

where, in agreement with the sketch in Fig. 5(a), $ikE_{in1}$ ($ikE_{in2}$) is the direct excitation of the left-side (right-side) input field and $\beta_{ij}$ is related to the surface roughness of the microresonator.

Considering a monochromatic incident field $E_{in} = E_{inc}\, e^{i\omega t}$, and, then, a direct excitation through only the left-side input port (i.e. using the coupled equations (4)), one can obtain an analytical expression of the transmission and reflection fields as:

$$t_{l-r} = 1 - \frac{2\Gamma\,(i\Delta\omega + \gamma + \Gamma)}{[i\Delta\omega + \gamma + \Gamma]^2 - (\beta_{12}\beta_{21})} \tag{6}$$

and

$$r_{l-r} = \frac{2\Gamma\,\beta_{21}}{[i\Delta\omega + \gamma + \Gamma]^2 - (\beta_{12}\beta_{21})}, \tag{7}$$

where $\Delta\omega = \omega_{inc} - \omega$ is the detuning frequency and $\Gamma = |k|^2/2$ is the radiative loss rate. The same derivation can be done by swapping the input ports and thus considering the coupled equations (5). In agreement with the optical reciprocity principle, the transmission from different directions (l-r and r-l) is the same $t_{r-l} = t_{l-r}$, while the reflection has the different form:

$$r_{r-l} = \frac{2\Gamma\,\beta_{12}}{[i\Delta\omega + \gamma + \Gamma]^2 - (\beta_{12}\beta_{21})}. \tag{8}$$

For a vanishing roughness $\beta_{i,j} = 0$, reflections in both (l-r and r-l) directions are equal to zero. The transmitted intensity assumes the conventional symmetric Lorentzian and, depending on the ratio of radiative $\Gamma$ to non-radiative $\gamma$ losses, three coupling regimes can be identified: critical- ($\Gamma = \gamma$), under- ($\Gamma < \gamma$) and over-coupling ($\Gamma > \gamma$).

### 4.1 Hermitian and Non-Hermitian Coefficients

In order to deal with the intra-cavity coefficients, and to condense the spectrum of solutions to few cases, let us introduce the following notation:

$$\begin{aligned} h &= i\,\frac{\beta_{12} - \beta_{21}^*}{2} \\ n &= \frac{\beta_{12} + \beta_{21}^*}{2}, \end{aligned} \tag{9}$$

where $h = |h|e^{i\theta}$ and $n = |n|e^{i\phi}$ are the Hermitian and non-Hermitian coefficients respectively. Their origin can be easily understood in the simplest case of counter-propagating modes $e^{\pm i\ell\varphi}$ perturbatively coupled by a single localized scatterer located at an angle $\varphi_0$ along the ring resonator and of complex potential $V_0$, whose real (imaginary) part is reactive (dissipative). In this case, the couplings $\beta_{12}$ ($\beta_{21}$ ) are proportional to $V_0 e^{2i\ell\varphi_0}$ (and $V_0 e^{-2i\ell\varphi_0}$). The complex-valued Hermitian and

non-Hermitian components $h \propto \mathrm{Re}[V_0]e^{2i\ell\varphi_0}$ and $n \propto \mathrm{Im}[V_0]e^{2i\ell\varphi_0}$ are related to the reactive and dissipative effects of the potential. Since the contribution of many scatterers adds up, it is immediate to see that no special relation holds between $\beta_{12}$ and $\beta_{21}$, which can then attain arbitrary and independent values.

The normalized difference between the r-l and l-r reflections depends only on the scatterers inside the microresonator and can be written as:

$$\frac{|\max(|r_{l-r}|^2) - \max(|r_{r-l}|^2)|}{\max(|r_{l-r}|^2, |r_{r-l}|^2)} = \frac{1}{\frac{|h|^2+|n|^2}{4|h\,n\,\sin(\Delta\Theta)|} + \frac{1}{2}}, \tag{10}$$

where $\Delta\Theta = \phi - \theta$. While this angle vanishes for a single scatterer, it can attain any value for more complex configurations with assemblies of scatterers. To give an idea of the variety of the possible behaviors, a tentative classification of the system response can be the following one:

- $\Delta\Theta = m\,\pi$ where $m \in \mathbb{Z}$: the coupled Eqs. 4 and 5 can be reduced to the same formulation. The reflection l-r is equal to the r-l one (i.e. Eq. 10 vanishes) but the transmission spectra can assume different doublet shape depending on the relative values of the Hermitian and non-Hermitian coefficients $|h|$ and $|n|$. In particular, for a purely reactive coupling $|n| = 0$, so that the intra-cavity coefficient satisfies $\beta_{12} = -\beta_{21}^*$ and the doublet is perfectly balanced. As already pointed out earlier in this work, the dissipative non-Hermitian processes play a central role in the system dynamics.
- $\Delta\Theta = (m + 1/2)\,\pi$ where $m \in \mathbb{Z}$: the reflection spectra between the l-r and r-l excitations are different but a perfectly balanced doublet exists in the transmission response. In the limiting case $|h| = |n|$ one of the two $\beta_{12}, \beta_{21}$ vanishes. Reflection then occurs in one direction only and transmission recovers a simple Lorentzian. In the $|n| = 0$ limit, this case reduces to the previous one with $\beta_{12} = -\beta_{21}^*$.
- $\Delta\Theta \neq m\,\pi$ and $\neq (m + 1/2)\,\pi$ with $m \in \mathbb{Z}$: both the transmission spectra display an unbalanced doublet and the reflections responses l-r and r-l are different.

In all cases the non-Hermitian coefficient $|n|$ is constrained by the intrinsic term $\gamma$, which takes into account the total losses of a propagating mode inside the microresonator. Both the material absorption and inter-modal mediated coupling losses contribute to the intrinsic parameter. While the Hermitian coefficient induces the mode splitting giving rise to a continuous exchange of the same energy between the CW and CCW mode, the presence of $n$ introduces a different balance between the reflection and inter-modal mediated coupling losses. Thus, $|n|$ has to be less than or equal to the intrinsic coefficient (i.e. $|n| \leq \gamma$) in order to avoid gain of the system. Summarizing, the repeated backscattering processes induced by scatterers randomly located on the surface affect the reflected light due to the presence of many interfering scattering and loss paths. As a result, an additional dissipative non-Hermitian coefficient has be considered. In the case of a multi-mode resonator, the effect is even stronger due to the additional couplings to other high order modes which enable additional loss channels. These further paths mediate the energy exchange between the CW and CCW modes, increasing the non-Hermitian (dissipative) character of the coupling (see Fig. 3).

As usual, the phase of the transmitted light is given by the argument of the transmission, Arg($t$). As we have seen in the experimental section, the phase and transmission responses can be put together into a phasor graph. This representation allows to exploit the inverse complex of the shifted field ($t - 1$), giving real and imaginary parts equal to:

$$\mathrm{Re}\left[\frac{1}{t-1}\right] = -\frac{\gamma + \Gamma - \mathrm{Re}[\eta_{int}]}{2\Gamma} \tag{11}$$

$$\mathrm{Im}\left[\frac{1}{t-1}\right] = -\frac{\Delta\omega - \mathrm{Im}[\eta_{int}]}{2\Gamma}, \tag{12}$$

where we have defined the short-hand

$$\eta_{int} = \frac{\beta_{12}\,\beta_{21}}{i\Delta\omega + \gamma + \Gamma}. \tag{13}$$

When the back-scattering couplings are zero ($\beta_{12} = \beta_{21} = 0$, then $h = n = 0$), the real part (11) is constant and its value is directly related to the intrinsic and extrinsic parameters. The imaginary part is proportional to the detuning $\Delta\omega$. This explains the experimental result for the single mode microresonator shown in Fig. 1(c) where a perfect circle maps to a straight line under the inversion. The utility of this procedure is particularly evident in Fig. 1(f1)-(f2) where the presence of a small contribution of the intra-cavity backcoupling parameter introduces an indiscernible perturbation of the symmetric Lorentzian or of the perfect circle in the phasor representation. However, this produces a noticeable peak on top of a straight line in the complex inverse shown in Fig. 1(f3).

Our simple analytical model can predict the experimental behaviour observed in Section 2. Both the acquired transmittivity and the transmission phase-shift spectra have been fitted simultaneously to remove the mutual dependence of the parameters: the quality of the fit can be appreciated on the phasor diagram of panels (c2–f2) which shows both the information encoded in the real and complex parts. The small differences between the fit and the data out of the resonance region is likely due to the weak Fabry-Perot cavity effect at the facets of the waveguide, an effect that is most visible far from the resonance region.

The experimental data of Fig. 1(c) require a zero value of the intra-cavity coupling coefficient: they match with a typical Lorentzian ($|h| = |n| = 0$ and $\Gamma/\gamma = 0.58$). The measurements of Fig. 1(d) exhibit a balanced doublet which can be reproduced by the second case of our classification: $|n|/|h| = 2 \cdot 10^{-2}$, $\Delta\Theta = -270$ degrees and $\phi = -90$ degrees with $\Gamma/\gamma = 0.54$. The balanced doublet is obtained by increasing the sample temperature. This introduces a shift of the bare frequency and then a change of the mode distribution inside the cavity [29]. The data of Fig. 1(e) show a certain degree of unbalance, as highlighted by the blue arrow in the transmittivity spectrum (Fig. 1(e1)). This behaviour falls in the third case of our classification and requires the simultaneous presence of Hermitian and non-Hermitian parts, $|n|/|h| = 0.13$, $\Delta\Theta = -193.63$ degree and $\phi = -13.64$ degrees with $\Gamma/\gamma = 0.24$.

In the case of the Fig. 1(f1) the presence of the doublet is hidden. The transmittivity could have been fitted also by a single resonance model with $|h| = |n| = 0$, see black-dashed line. Even though the phasor diagram in Fig. 1(e2) shows the same fit uncertainty for the two cases, the ambiguity is resolved by the complex inverse representation, as shown in Fig. 1(e3). In this diagram, the small difference between the perfect circle of a single resonance and the experimental data is clear. The hidden doublet corresponds to the following intra-cavity coupling parameters: $|n|/|h| = 0.16$, $\Delta\Theta = -270$ degrees and $\phi = -90$ degrees with $\Gamma/\gamma = 0.37$. This experimental configuration falls into the second case of our classification and the small contribution of the intra-cavity coefficients introduces a clear peak on top of the straight line in the complex inverse representation.

A further confirmation of this analytical model comes from the comparison with the numerical simulations. A stringent test in this direction can be performed as follows. The doublets in the transmission (Fig. 4(a1)–(c1)) and l-r reflection (Fig. 4(a2)–(c2)) spectra are simultaneously fitted by using the Eqs. 6–7 (red lines). Then, the fit parameters obtained in this way are inserted in Eq. 8 to obtain a prediction for the r-l reflectivity (green lines in Fig. 4(a3)–(c3)). The perfect match of this prediction with the numerical data is a strong evidence that the analytical model is capturing the main points of the physics. In particular, it turns out that Fig. 4(a) corresponds to an almost balanced doublet with a slight difference in the l-r and r-l reflections. This behaviour corresponds to intra-cavity parameters resembling the second case of our classification with $|n|/|h| = 1 \cdot 10^{-2}$, $\Delta\Theta = -90$ degrees and $\phi = 90$ degree and $\Gamma/\gamma = 0.82$. On the other hand, the simulation results of Fig. 4(b)–(c) belong to the third case with $|n|/|h| = 0.41$, $\Delta\Theta = -64.93$ degree and $\phi = 114.19$ degrees and $\Gamma/\gamma = 0.59$ in the former case; $|n|/|h| = 0.87$, $\Delta\Theta = 247.42$ degrees and $\phi = 136.48$ degree and $\Gamma/\gamma = 0.74$ in the latter case.

## 5. Conclusion

In this work we have provided experimental, numerical, and analytical evidences that the surface roughness due to the fabrication process can be the origin of an unbalanced doublet in the transmission spectra for a microdisk resonator coupled to a bus-waveguide. The experimental spectra

are well explained by a simple model including conservative as well as dissipative couplings between the counter-propagating modes due to the roughness. While optical reciprocity imposes that the transmittivities in the two directions are equal, we anticipate that the stochastic roughness and the dissipative couplings should give rise to a marked asymmetry in the reflectivities, as shown by the numerical simulations and the analytical model.

## Acknowledgment

The authors would like to thank A. Calabrese, M. Borghi, A. Trenti, G. Abbiati, J. Lebreuilly, and M. Flaim for their helpful comments and discussions, and E. Moser for his technical support.

*Author contribution:* Both S. Biasi and F. Ramiro-Manzano conceived and have made a substantial and equal contribution to all the stages of the study, including writing the paper. F. Turri has participated in the experiment. Mher Ghulinyan has designed and fabricated the samples. Pierre-Élie Larré has contributed in the theoretical phase extrapolation. I. Carusotto was the theoretical supervisor and L. Pavesi was in charge of the general supervision of the work and contributed to the text.

## References

[1] J. Kerry and K. J. Vahala, "Optical microcavities," *Nature*, vol. 424, pp. 839–846, 2003.
[2] F. Vollmer and L. Yang, "Label-free detection with high-Q microcavities: A review of biosensing mechanisms for integrated devices," *Nanophotonics*, vol. 1, pp. 267–291, 2012.
[3] A. Samusenko *et al.*, "A SiON microring resonator-based platform for biosensing at 850 nm," *J. Lightw. Technol.*, vol. 34, no. 3, pp. 969–977, Feb. 2016.
[4] T. Udem, R. Holzwarth, and T. W. Hänsch, "Optical frequency metrology," *Nature*, vol. 416, pp. 233–237, 2002.
[5] S. B. Papp *et al.*, "Microresonator frequency comb optical clock," *Optica*, vol. 1, pp. 10–14, 2014.
[6] J. Müller *et al.*, "Optical peaking enhancement in high-speed ring modulators," *Nature Photon.*, *Sci. Rep.*, vol. 4, 2014, Art. no. 6310.
[7] S. Amiri and A. Afroozeh, *Ring Resonator Systems to Perform Optical Communication Enhancement Using Soliton*. Berlin, Germany: Springer, 2015.
[8] J. E. Heebner and R. W. Boyd, "SLOW AND STOPPED LIGHT 'Slow' and 'fast' light in resonator-coupled waveguides," *J. Modern Opt.*, vol. 49, pp. 2629–2636, 2002.
[9] P. D. Haye, A. Schliesser, O. Arcizet, T. Wilken, R. Holzwarth, and T. J. Kippenberg, "Optical frequency comb generation from a monolithic microresonator," *Nature*, vol. 450, pp. 1214–1217, 2007.
[10] J. W. Silverstone *et al.*, "Qubit entanglement between ring-resonator photon-pair sources on a silicon chip," *Nature Commun.*, vol. 6, pp. 1214–1217, 2015.
[11] C. Reimer *et al.*, "Generation of multiphoton entangled quantum states by means of integrated frequency combs," *Science*, vol. 351, pp. 1176–1180, 2016.
[12] J. Heebner, R. Grover, and T. Ibrahim, *Optical Microresonator Theory, Fabrication and Applications*. Berlin, Germany: Springer, 2008.
[13] H. Lee *et al.*, "Chemically etched ultrahigh-Q wedge-resonator on a silicon chip," *Nature Photon.*, vol. 6, pp. 369–373, 2012.
[14] X. Ji *et al.*, "Ultralow-loss on-chip resonators with sub-milliwatt parametric oscillation threshold," *Optica*, vol. 4, pp. 619–624, 2017.
[15] W. Bogaerts *et al.*, "Silicon microring resonators," *Laser Photon. Rev.* vol. 6, pp. 47–73, 2012.
[16] T. J. Kippenberg, S. M. Spillane, and K. J. Vahala, "Modal coupling in traveling-wave resonators," *Opt. Lett.*, vol. 27, pp. 1669–1671, 2002.
[17] A. Li, T. V. Vaerenbergh, P. D. Heyn, P. Bienstman, and W. Bogaerts, "Backscattering in silicon microring resonators: a quantitative analysis," *Laser Photon. Rev.*, vol. 10, pp. 420–431, 2016.
[18] M. Borselli, T. J. Johnson, and O. Painter, "Beyond the Rayleigh scattering limit in high-Q silicon microdisks: Theory and experiment," *Opt. Exp.*, vol. 13, pp. 1515–1530, 2005.
[19] Q. Li, Z. Zhang, J. Wang, M. Qiu, and Y. Su, "Fast light in silicon ring resonator with resonance-splitting," *Opt. Exp.*, vol. 17, pp. 933–940, 2009.
[20] Z. Zhang, M. Dainese, L. Wosinski, and M. Qiu, "Resonance-splitting and enhanced notch depth in SOI ring resonators with mutual mode coupling," *Opt. Exp.*, vol. 16, pp. 4621–4630, 2008.
[21] B. Peng *et al.*, "Chiral modes and directional lasing at exceptional points," *Proc. Nat. Acad. Sci.* vol. 113, pp. 6845–6850, 2016.
[22] J. Wiersig, "Structure of whispering-gallery modes in optical microdisks perturbed by nanoparticles," *Phys. Rev. A*, vol. 84, 2011, Art. no. 063828.
[23] A. Mazzei, S. Götzinger, L. de S. Menezes, G. Zumofen, O. Benson, and V. Sandoghdar, "Controlled coupling of counterpropagating whispering-gallery modes by a single Rayleigh scatterer: A classical problem in a quantum optical light," *Phys. Rev. Lett.*, vol. 99, 2007, Art. no. 173603.

[24] M. Kim, K. Kwon, J. Shim, Y. Jung, and K. Yu, "Partially directional microdisk laser with two rayleigh scatterers," *Opt. Lett.*, vol. 39, pp. 2423–2426, 2014.
[25] L. D. Bino, J. M. Silver, S. L. Stebbings, and P. Del'Haye, "Symmetry breaking of counter-propagating light in a nonlinear resonator," *Sci. Rep.*, vol. 7, 2017 Art. no. 43142.
[26] F. Ramiro-Manzano, N. Prtljaga, L. Pavesi, G. Pucker, and M. Ghulinyan, "A fully integrated high-Q whispering-gallery wedge resonator," *Opt. Exp.*, vol. 20, pp. 22934–22942, 2012.
[27] A. Trenti *et al.*, "Thermo-optic coefficient and nonlinear refractive index of silicon oxynitride waveguides," *AIP Adv.*, vol. 8, 2018, Art. no. 025311.
[28] F. Turri, S. Biasi, F. R. Manzano, and L. Pavesi, "A free-space interferometer for phase-delay measurements in integrated optical devices in degenerate pump-and-probe experiments," *IEEE Trans. Instrum. Meas.*, pp. 1–9, 2018, doi: 10.1109/TIM.2018.2830845.
[29] F. Ramiro-Manzano, S. Biasi, F. Turri, P. Larré, M. G. I. Carusotto, and L. Pavesi, "Non-linear thermo-optic effect on the asymmetric mode splitting in a microdisk resonator," *to be published*.
[30] L. Snchez-Soto, J. Monzn, and G. Leuchs, "The many facets of the Fabry–Perot," *Eur. J. Phys.*, vol. 37, 2016, Art. no. 064001.
[31] T. Needham, *Visual Complex Analysis.* London, U.K.: Oxford Univ. Press, 1997.
[32] S. Manna *et al.*, "Multi-mode interference revealed by two photon absorption in silicon rich $SiO_2$ waveguides," *Appl. Phys. Lett.*, vol. 106, 2015, Art. no. 071109.
[33] M. Ghulinyan *et al.*, "Inter-mode reactive coupling induced by waveguide-resonator interaction," *Phys. Rev. A*, vol. 90, 2014, Art. no. 053811.
[34] S. Fan, W. Suh, and J. Joannopoulos, "Temporal coupled-mode theory for the Fano resonance in optical resonators," *J. Opt. Soc. Amer. A*, vol. 20, pp. 569–572, 2003.
[35] D. Walls and G. Milburn, *Quantum Optics.* Berlin, Germany: Springer, 1994.
[36] B. E. Little, S. T. Chu, H. A. Haus, J. Foresi, and J.-P. Laine, "Microring resonator channel dropping filters," *J. Lightw. Technol.*, vol. 15, no. 6, pp. 998–1005, Jun. 1997.
[37] W. Suh, Z. Wang, and S. Fan, "Temporal coupled-mode theory and the presence of non-orthogonal modes in lossless multimode cavities," *IEEE J. Quantum Electron.*, vol. 40, no. 10, pp. 1511–1518, Oct. 2004.